

Controlling Particle/Metal Interactions in Metal Matrix Composites During Solidification: The Role of Melt Viscosity and Cooling Rate



RENHAI SHI, JANET M. MEIER, and ALAN A. LUO

The homogenous dispersion of particles in a metal matrix is of critical importance to the design and manufacturing of particle-reinforced metal matrix composites (MMCs). This work studied the effects of increasing melt viscosity *via* microalloying and increasing cooling rate on the dispersion of particles in an aluminum-based MMC. A CALculation of PHase Diagrams (CALPHAD)-based viscosity model was developed for the Al-Ni binary system. This viscosity model was coupled with a particle-capture model to explore particle/metal interactions during solidification. Three composites (Al + TiC_p) with and without Ni were cast at different cooling rates. The first composite without Ni cast at a lower cooling rate showed macro-segregation and agglomeration of TiC_p along the grain boundaries. The second composite without Ni cast at a higher cooling rate exhibited grain refinement and reduced macro-segregation of TiC_p. The third composite alloyed with 1 wt pct Ni and cast at the same higher cooling rate had an improved distribution, and particles > 2 μm in size were captured in the grains. The composite with 1 wt pct Ni had a 45 pct higher melt viscosity and a 31 pct lower critical velocity for capture of TiC_p, demonstrating a synergetic effect of increasing viscosity and cooling rate on improving particle dispersion in MMCs.

<https://doi.org/10.1007/s11661-019-05307-9>

© The Minerals, Metals & Materials Society and ASM International 2019

I. INTRODUCTION

LIGHTWEIGHT materials have shown increasing applications for energy efficiency^[1] in the aerospace^[2] and automotive^[3,4] industries. Advanced light alloys, such as Al alloys^[5,6] and Mg alloys,^[7,8] have been developed by optimizing alloy compositions and manufacturing processes with computational and experimental approaches.^[9] One effective approach to further improve the performance of light alloys is to introduce ceramic reinforcements (*e.g.*, particles and fibers) to produce metal matrix composites (MMCs).^[10–16] In order to obtain a homogeneous distribution of ceramic reinforcements in a MMC, there are two required conditions. First, the ceramic particles/fibers must be uniformly dispersed in the liquid metal.^[17–19] Second, the particles/fibers must be captured and engulfed by the solidification front during processing.^[20–22]

It is particularly challenging to capture particles of small size, such as micron to nano-scale, during solidification in conventional casting conditions. For example, the solidification cooling rate in MMC casting is often not high enough to capture particles within the grain/dendrite interiors and the particles are pushed to grain boundaries or inter-dendritic regions. One way to improve capture is to increase the solidification cooling rate so the velocity of the solidification front is higher than the moving velocity of the particles.^[20–22] In this paper, we propose an approach to increase the melt viscosity to decrease the moving velocity of particles so capture can occur at lower cooling rates. The benefit of this approach is that the viscosity of a MMC melt can be modified *via* microalloying. However, one important gap in understanding the influence of microalloying on the particle/metal interactions during solidification is the lack of composition/temperature-dependent thermo-physical parameters, such as viscosity, for multi-component alloy systems. So far, theoretical models^[20–22] dealing with such influences only used viscosity values for pure metals due to the complexity and difficulty of measurements for multi-component alloy systems.

It is critical to construct a theoretical model for the viscosity of multi-component alloy systems to understand and optimize the solidification processing of MMCs. However, previous theoretical viscosity

RENHAI SHI and JANET M. MEIER are with the Department of Materials Science and Engineering, The Ohio State University, Columbus, OH, 43210. ALAN A. LUO is with the Department of Materials Science and Engineering, The Ohio State University and also with the Department of Integrated Systems Engineering, The Ohio State University, Columbus, OH, 43210. Contact e-mail: luo.445@osu.edu

Manuscript submitted January 21, 2019.

Article published online June 5, 2019

models^[23–25] for multi-component alloy systems only include thermodynamic parameters, but not the non-ideal mixing behavior corresponding to chemical short-range order. In this work, we first developed a new theoretical particle-capture model coupled with our CALPHAD-based viscosity model. The viscosity of the pure Ni melt was estimated using the Arrhenius law with available viscosity data^[26–32] and the viscosity of the Al-Ni binary melt system was assessed using the PARROT module in the Thermo-Calc software with available experimental data.^[33–37] Then, we experimentally investigated and theoretically analyzed the dispersive behavior of TiC_p during the solidification of MMC melts with various cooling rates (as seen in sand and permanent mold casting) and melt viscosities by microalloying with 1 wt pct Ni.

II. MODELING AND EXPERIMENTAL PROCEDURES

A. Coupled Viscosity and Particle-Capture Model

In this section, a new particle-capture model coupled with a CALPHAD-based viscosity model has been developed to describe the interfacial behavior of ceramic particles during the solidification of MMCs. In the model, these ceramic particles are assumed to be spherical and homogeneously distributed in a static metal/alloy melt. During the process of solidification, the solidification front (liquid–solid interface) is assumed to be non-flat, as shown in Figure 1. The solidification front near a ceramic particle could be concave or convex based on differences in the thermal conductivity between the ceramic particles and the alloy melt. The buoyancy and gravity forces are considered to be negligible for nano/submicron scale particles and are not considered in this model. The electrostatic interactions between the ceramic particle, melt, and solidified alloy matrix are neglected because the melt and the solidified alloy matrix are electrically neutral. Flow due to convection between the solidification front and the melt is also not considered. No severe chemical reactions occur between the ceramic particles and melt. The engulfment of the ceramic particle by the solidification front will be determined by two criteria: the thermodynamic criterion and the kinetic criterion. When both criteria are satisfied, the ceramic particle should be captured and engulfed by the solidification front. Otherwise, the ceramic particle will be pushed away from solidification front and entrapped along the grain boundaries.

1. Thermodynamic Criterion

During solidification (Figure 1), the forces acting on a particle will vary based on the distance (d) between the solidification front and the ceramic particle. When d is between 0.2 to 0.4 nm, chemical bonds between the ceramic particles and the solid metal surface^[22] will be formed and the interfacial energy will dominate. Thus, the Gibbs energy for a ceramic particle moving from the melt into the solidified alloy matrix can be described as

$$\Delta G = 4\pi r^2(\gamma_{ps} - \gamma_{pl}), \quad [1]$$

where r is the particle radius, γ_{ps} and γ_{pl} are interfacial energies between the ceramic particle and the solidified alloy matrix and melt, respectively. If ΔG is less than zero ($\gamma_{ps} < \gamma_{pl}$), the ceramic particle will be more thermodynamically stable in the solidified alloy matrix and the ceramic particle will be engulfed by solidification front. If $\Delta G > 0$, the particle will be pushed away from the solidification front. Thus, the thermodynamic prerequisite of engulfing a ceramic particle during solidification is to satisfy $\Delta G < 0$ when d is less than 0.4 nm.

2. Kinetic Criterion

When the distance (d) between a ceramic particle and the solidification front is larger than 0.4 nm, the van der Waals potential will have the dominant effect on particle motion during solidification. The van der Waals force (F_{vdw}) was derived from the van der Waals potential (W_{vdw}) from Potschke *et al.*^[38] and modified by Shang-guan *et al.*^[20] and can be given by

$$\begin{aligned} F_{vdw} &= -\frac{\partial W_{vdw}}{\partial d} \\ &= -\frac{32}{3} \\ &A \frac{r^3 r_1^3 (r_1 - r - a_0 - d)}{(a_0 + d)^2 (a_0 + d + 2r)^2 (a_0 + d - 2r_1)^2 (a_0 + d - 2r_1 + 2r)^2}, \end{aligned} \quad [2]$$

where A is the Hamaker constant, r is the radius of the ceramic particle, r_1 is the radius of curvature of the solidification front near the ceramic particle, and a_0 is the characteristic decay length for the chemical bonds between the ceramic particle and the solidified alloy matrix (0.2 to 0.4 nm). In this study, $a_0 + d \ll r$ and $a_0 + d \ll r_1$. Thus, the van der Waals force (F_{vdw}) can be simplified as

$$F_{vdw} = -\frac{A}{6} \frac{r r_1}{(a_0 + d)^2 (r_1 - r)} = -\frac{A r \alpha}{6(a_0 + d)^2}, \quad [3]$$

where $\alpha = \frac{k_p}{k_l}$ is the ratio of the thermal conductivity of the ceramic particle (k_p) to the melt (k_l). Shang-guan *et al.*^[20] determined that $\frac{r_1}{(r_1 - r)} = \alpha$ which allows for further simplification.

In the ceramic particle-melt-solidified alloy matrix system, the system Hamaker constant (A) can be expressed as^[39]

$$A = \left(\sqrt{A_S} - \sqrt{A_L} \right) \left(\sqrt{A_{NP}} - \sqrt{A_L} \right), \quad [4]$$

where A_{NP} , A_S , and A_L are the Hamaker constants for the ceramic particle, solidified alloy matrix, and melt, respectively. Generally, A_S is larger than A_L because the solid metal has a higher plasma frequency.^[22] If $A_{NP} > A_L$, the system Hamaker constant (A) is greater than zero and thus $F_{vdw} < 0$ (Eq. [3]). If $F_{vdw} < 0$, it acts as an attractive force and the ceramic particle will spontaneously approach the advancing solidification front. If $A_{NP} < A_L$, $F_{vdw} > 0$ and acts as a repulsive

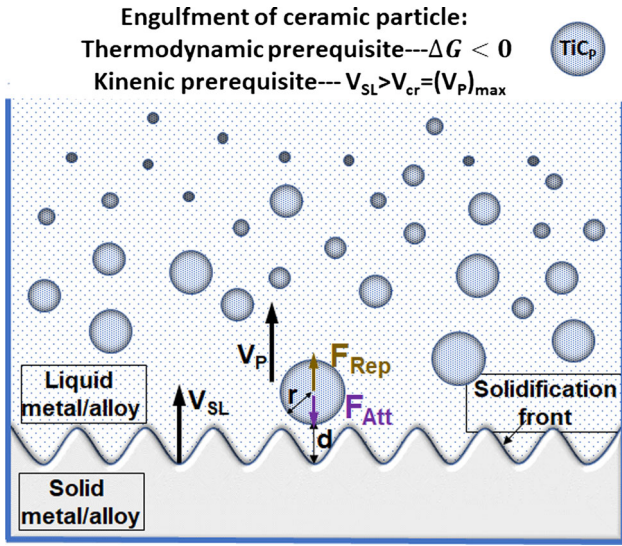


Fig. 1—Schematic illustration of interactions between a ceramic particle and the metal solidification front during solidification. TiC_p denotes a ceramic particle, d denotes the distance between the ceramic particle and the solidification front, r is the radius of the ceramic particle, F_{Rep} is the repulsive force acting on the ceramic particle, F_{Att} is the attractive force acting on the ceramic particle, V_{SL} and V_p are the advancing velocities of the solidification front and ceramic particle, respectively, and V_{cr} is the maximum particle velocity during solidification.

force to push the ceramic particle away from the advancing solidification front. In this study, the influence of dilute alloy solutes on the constant A will not be considered due to small amount of added alloying element and lack of experimental information. As the ceramic particle moves in the melt at a velocity V_p , a viscous drag force is generated. The magnitude of this drag force is given by Stokes's law,^[40]

$$F_D = 6\pi\eta r V_p, \quad [5]$$

where η is the viscosity of the bulk melt and r is the radius of the ceramic particle. When the solidification front is approaching the ceramic particle, the influence of d on the viscous drag force (F_D) was derived by Shangguan *et al.*^[20] to be

$$F_D = 6\pi\eta V_p \frac{r^2}{d} \alpha^2. \quad [6]$$

Based on previous studies, the viscosity (η) of the melt around a particle is affected by various factors.

First, Chan *et al.*^[41] observed that the viscosity $\eta_{eff}(d)$ of the melt around a particle will be different from the viscosity η_{bulk}^0 of the bulk melt and proposed the effective viscosity as

$$\eta_{eff}(d) = \eta_{bulk}^0 \frac{d}{d - 2a_0}, \quad [7]$$

where $2a_0 < d < 50$ nm. When $d < 2a_0$, the viscosity approaches infinity and the liquid is considered to behave as a solid. Also, the viscosity η_{bulk}^0 of the bulk melt is affected by the alloying elements, temperature, and volume fraction of particles, which will be studied by CALPHAD-based model as well as by Einstein–Batchelor model^[42] in this study.

Alloying elements have a significant effect on the viscosity η_{bulk}^0 of a bulk melt system. The following CALPHAD-based viscosity model was developed to accurately calculate the viscosity η'_{bulk} of an alloying melt system by introducing non-idea mixing of solutes in the liquid.

$$\eta'_{bulk} = \sum_i x_i \eta_{bulk,i}^0 + \eta^{EX} \quad [8]$$

$$\eta_{(bulk,i)}^0 = \eta_0 \exp\left(\frac{E_a^0}{RT}\right) \quad [9]$$

$$\eta^{EX} = \sum_{j,k \neq j}^i x_j x_k L_{j,k}^{EX} \quad [10]$$

$$L_{(j,k)}^E X = \sum_{(n=0)}^m (a_n + b_n T)(x_1 - x_2)^n, \quad [11]$$

where $\eta_{bulk,i}^0$ is the viscosity of a pure liquid metal which obeys the Arrhenius law (η_{AL} was adopted from^[43] in this work), x_i is the mole fraction of component i , and η^{EX} is the excess viscosity contribution from non-ideal mixing of solutes in the melt system expressed with the Redlich–Kister polynomial.^[44] η_0 is the pre-exponential viscosity at very high temperatures and E_a^0 is the activation energy of viscous flow. Both are constants and can be fitted with available experimental data. R is the universal gas constant and T is the absolute temperature. $L_{j,k}^{EX}$ is the interaction parameters between components j and k . a_n and b_n are constants and are optimized on the basis of available experimental data by using the PARROT module of the Thermo-Calc software.

The effect of the volume fraction of ceramic particles on the viscosity η'_{bulk} of the alloying melt is considered using the Einstein–Batchelor model^[42]:

$$\eta''_{bulk} = \eta'_{bulk} \left(1 + 2.5\phi_p + 6.2\phi_p^2\right), \quad [12]$$

where ϕ_p is volume fraction of ceramic particles suspended in the melt system.

Therefore, the combination of Eqs. [7] through [12] can be used to determine the viscosity $\eta_{eff}(d)$ of the melt around a particle in an alloy system and the final viscous drag force (F_D) can be determined by replacing the viscosity with the final viscosity from Eq. [13],

$$\eta_{\text{eff}}(d) = \left(\sum_i x_i \eta_{\text{bulk},i}^0 + \eta^{\text{EX}} \right) \frac{d}{d-2a_0} \left(1 + 2.5\phi_p + 6.2\phi_p^2 \right) \quad [13]$$

$$F_D = 6\pi \left(\sum_i x_i \eta_{\text{bulk},i}^0 + \eta^{\text{EX}} \right) \frac{d}{d-2a_0} \left(1 + 2.5\phi_p + 6.2\phi_p^2 \right) V_p \frac{r^2}{d} \alpha^2. \quad [14]$$

As the solidification front approached a ceramic particle, the F_D acting on the ceramic particle is initially zero since the initial velocity of the particle is zero. The balance of the larger repulsive van der Waals force (F_{vdw}) and the smaller attractive viscous drag force (F_D) will initially increase the velocity (V_p) of the ceramic particle away from the solidification front. As V_p increases the viscous drag force (F_D) (Eq. [14]) will be further increased until the balance between F_{vdw} and F_D is zero. In this case, the ceramic particle moves in the melt at a steady velocity, V_e .

$$F_{\text{vdw}} = F_D \quad [15]$$

$$V_e = \frac{-A(d-2a_0)}{36\pi r \alpha (a_0 + d)^2 \left(\sum_i x_i \eta_i + \eta^{\text{EX}} \right) \left(1 + 2.5\phi_p + 6.2\phi_p^2 \right)} \quad [16]$$

The steady velocity (V_e) of the ceramic particle will be different based on variations in the distance (d) between the ceramic particle and the advancing solidification front. The maximum steady velocity (V_{cr}) can be obtained at a critical distance d_{cr}

$$\left. \frac{\partial V_e}{\partial d} \right|_{d=d_{\text{cr}}} = 0 \quad [17]$$

$$d_{\text{cr}} = 5a_0 \quad [18]$$

$$V_{\text{cr}} = (V_e)_{\text{max}, d=d_{\text{cr}}} = \frac{(\sqrt{A_S} - \sqrt{A_L})(\sqrt{A_{\text{NP}}} - \sqrt{A_L})}{432\pi \left(\sum_i x_i \eta_i + \eta^{\text{EX}} \right) r \alpha a_0 \left(1 + 2.5\phi_p + 6.2\phi_p^2 \right)}. \quad [19]$$

For engulfment of the ceramic particle by the solidification front to occur, the solidification front must be able to get close enough to the ceramic particle so that the distance between them is in the 0.2 to 0.4 nm range for the thermodynamic criterion. Thus, the velocity (V_{SL}) of solidification front should be larger than the maximum velocity (V_{cr}) of ceramic particle before the end of solidification or when the solidification front meets another growing grain. This is the kinetic criterion for the engulfment of ceramic particles. In this study, the

pure metal matrix Hamaker constants A_S and A_L will be used and the effect of microalloying will not be considered due to the lack of available data in literature. The velocity of the solidification front is described using the well-known relationship.^[45]

$$V_{\text{SL}} = \dot{\epsilon}/G, \quad [20]$$

where $\dot{\epsilon}$ is the cooling rate in °C/s and G is the temperature gradient in °C/cm.

B. Experimental Procedure

In this work, three Al composites with TiC_p (~18 vol pct) were prepared to study the effects of microalloying with Ni and cooling rate on the particle/metal interactions during solidification. The first composite was pure Al + TiC_p . It was melted in a graphite crucible using an induction furnace and cast into a cylindrical steel die with a diameter of ~3 cm to produce a lower cooling rate. The second sample was pure Al + TiC_p cast into a cylindrical steel die with a diameter of ~1 cm. The third composite was pure Al + TiC_p with an addition of 1 wt pct Ni. It was prepared by melting the Al + TiC_p composite with an Al-20 wt pct Ni master alloy and was cast in the cylindrical steel die with a diameter of ~1 cm. K-type thermocouples were placed at center and edge positions of each steel cylinder die to measure the cooling curves during solidification. The average solidification properties including cooling rate, temperature gradient, and corresponding solidification rates were derived from the cooling curves. These three composites were machined and mechanically polished for microstructural characterization. Scanning electron microscopy (SEM) and energy-dispersive X-ray spectroscopy (EDS) analysis were carried out in a FEI Apreo SEM, operated at 20 kV and 30 kV. The size distribution of TiC_p in the pure Al + TiC_p sample was measured from the SEM backscattered electron images using Image Pro Plus. A dozen photographs with about 1700 particles were randomly selected for the quantitative analysis.

III. RESULTS AND DISCUSSION

A. Model Analysis

In this work, the dispersive mechanism for TiC_p in an aluminum matrix composite was studied using a particle-capture model coupled with a CALPHAD-based viscosity model. The interfacial energies, γ_{ps} and γ_{pl} , for the system are reported to be 0.77 J/m² and 0.81 J/m², respectively.^[46] The resulting Gibbs energy change for the system (Eq. [1]) was determined to be less than zero. Since $\Delta G < 0$, the TiC_p particles are more thermodynamically stable in the solidified alloy matrix than the alloy melt. Thus, TiC_p meets the thermodynamic criterion and should be engulfed when the solidification front is within 0.2 to 0.4 nm of the TiC_p particles.

In order for the solidification front to catch up with a particle, one of two approaches can be used. One is to decrease the maximum velocity (V_{cr}) of the particle, and

Table I. Parameters for Calculation of the Maximum Velocity of TiC_p in Pure Al/Al-Ni Alloys

| MMC System | a_0 ^[22] (m) | η (mPa S) | A_{solid} ^[47] (J) | A_{melt} ^[48] (J) | A_{TiC} ^[49] (J) | r (nm) | k_p ^[50] (W/Km) | k_L ^[51] (W/Km) | ϕ_p |
|---|---------------------------|---------------------------------|--|---------------------------------------|--------------------------------------|----------|------------------------------|------------------------------|----------|
| Al-TiC _p Al-1 wt pctNi-TiC _p | 2.0e-10 | from present viscosity model | 3.33E-19 | 2.66E-19 | 2.38E-19 | 200-1500 | 5.64 | 109.5 | 18 pct |

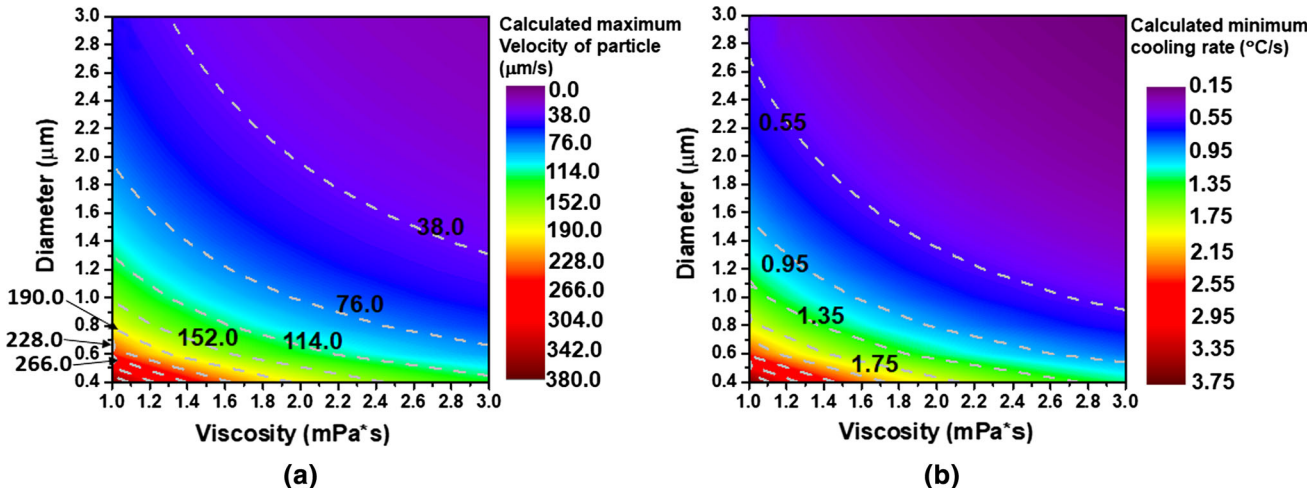


Fig. 2—(a) Calculated maximum velocity (V_{cr}) of TiC_p with different particle sizes and viscosity of liquid around particle in solidification. (b) Calculated corresponding critical cooling rate with constant temperature gradient ($G = 100$ °C/ cm). (For interpretation of the references to color in this Figure, the reader is referred to the web version of this article).

the other is to increase the velocity (V_{SL}) of the solidification front. The kinetic criterion for particle engulfment is that the maximum velocity (V_{cr}) of the particle should be less than the velocity (V_{SL}) of solidification front ($V_{cr} < V_{SL}$). Thus, the maximum velocity (V_{cr}) of the particle must be equal to the minimum velocity (V_{SL}) of the solidification front to derive the minimum cooling rate *via* Eq. [20]. The particle-capture model shown in Eq. [19] was proposed to estimate the maximum velocity (V_{cr}) of the particle during solidification. Based on Eq. [19], using the parameters^[47-51] listed in Table I, the maximum velocities (V_{cr}) of TiC_p particles during solidification were calculated and are shown in Figure 2(a). The maximum velocity (V_{cr}) of a particle can be significantly decreased by slightly increasing the melt viscosity. Thus, modifying the viscosity of the liquid around the particles is a promising approach to improve particle capture. The corresponding minimum cooling rate was calculated in Figure 2(b). It should be noted that the calculated minimum cooling rate was significantly higher for smaller particle sizes and lower liquid viscosities. Thus, this calculation could provide the required minimum cooling rate to experimentally manufacture MMCs with a known particle size and liquid viscosity.

A CALPHAD-based model (Eq. [8]) was used to select Ni as a potential microalloying element that can be used to increase the melt viscosity and to calculate the

viscosity of the resulting alloy. Based on the viscosity model, the calculated viscosity of a pure Ni liquid is shown in Figures 3(a) and (b) and the calculated viscosity of the binary Al-Ni liquid is shown in Figures 3(c) and (d). The calculated results had good agreement with available experimental viscosity data.^[26-37] The melting temperatures for the pure Ni and binary Al-Ni systems were calculated using the Thermo-Calc software with the TCAL5 thermodynamic database.^[52] The calculated pre-exponential viscosities and activation energies of pure liquid Ni are shown in Table II. The binary interaction parameters $L_{j,k}^{EX}$, from Eq. [11], for the binary Al-Ni liquid system have been assessed and are shown in Table III.

Figure 4(a) shows the calculated viscosities of the Al-Ni binary system just above the liquidus temperature using the present viscosity model. In the Al-rich corner, a small amount of Ni significantly increases the viscosity of the Al melt. Also, along the liquidus boundary two maxima were observed at points A (Al₈₄Ni₁₆, at.pct) and B (Al₂₅Ni₇₅, at.pct), which correspond to the formation of the Al₃Ni and FCC_L12 intermetallics, respectively. A similar phenomenon was observed in the calculations of solute diffusivity for Ni and Al in the Al-Ni liquid, as shown in Figures 4(b) and (c). The diffusivities were calculated using an experimentally validated diffusivity database^[53] for the Al-Ni binary liquid. The observed

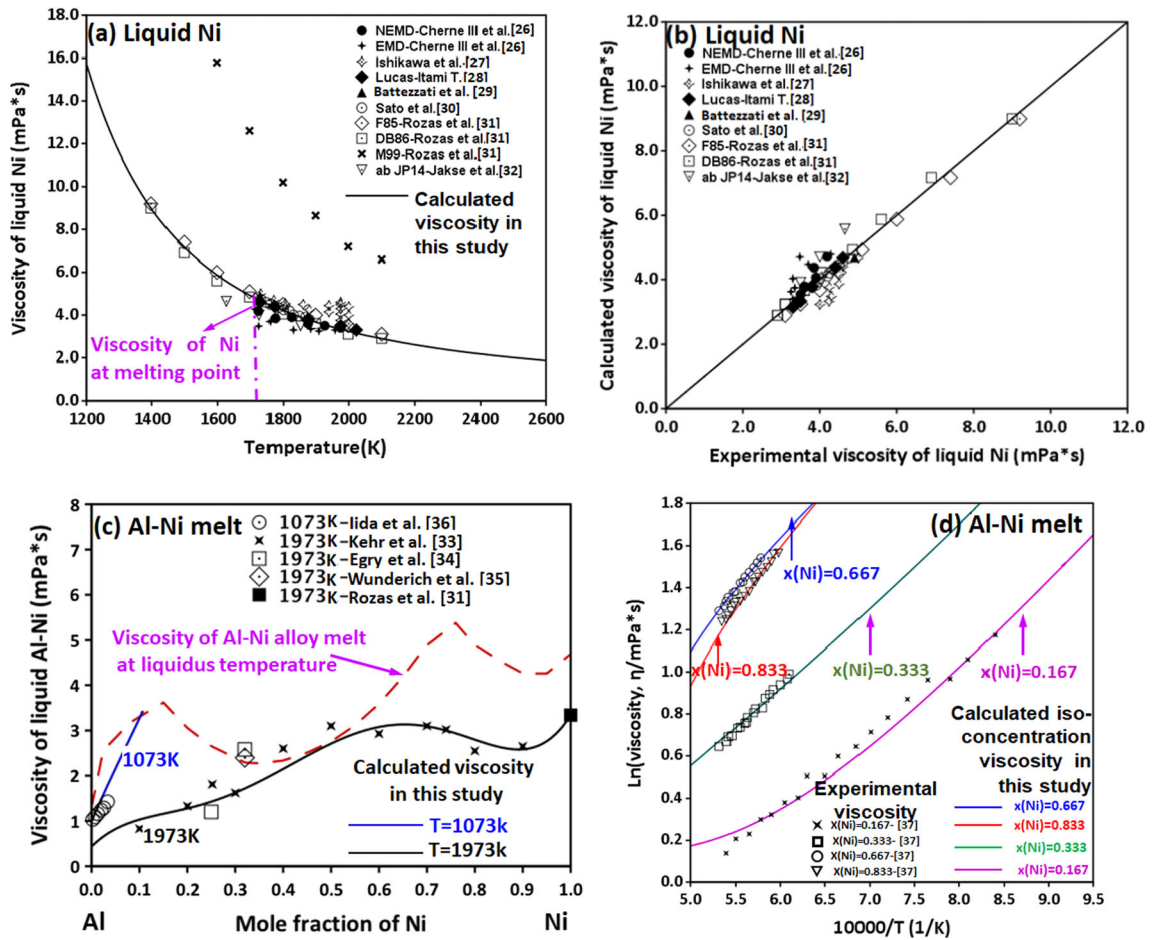


Fig. 3—(a) Calculated temperature-dependent viscosity of the pure Ni melt superimposed with experimental and theoretical data.^[26–32] (b) Comparison of the calculated viscosity of liquid Ni with experimental and theoretical data.^[33–37] (c) Calculated isothermal viscosity of the Al-Ni binary melt superimposed with experimental data^[33–37] at temperatures of 1073 K and 1973 K. (d) Calculated iso-concentration viscosity of the Al-Ni melt at compositions of $x(\text{Ni}) = 0.167, 0.333, 0.667,$ and 0.833 . Dashed lines in (a) and (c) denote the viscosities at liquidus temperature, which were calculated *via* Thermo-Calc software with the reliable thermodynamic database TCAL5.^[52]

Table II. Calculated and Experimental Viscosity Data for the Pure Ni Melt in this Study

| Metal | T_m (K) | η (T_m) (mPa s) | η_i^0 (mPa s) | E_i (10^4 J/mol) | References |
|-------|-----------|--------------------------|--------------------|-----------------------|--------------|
| Ni | 1728.25 | 4.70 | 0.301 | 3.95 | present work |
| | 1728 | 4.70 | 0.79 | 2.73 | 27 |
| | 1728 | 4.61 | 0.49 | 3.22 | 28 |
| | 1728.15 | 4.90 | 0.166 | 5.02 | 29 |
| | 1728 | 4.70 | 0.27 | 4.13 | 30 |

Table III. Interaction Parameters for the Viscosity of the Al-Ni Binary Liquid Assessed in this Study

| Parameters (mPa s) | Al-Ni | |
|--------------------|---------|------------|
| | A | b |
| $A_{j,k}^0$ | 14.560 | -5.733E-03 |
| $A_{j,k}^1$ | -34.502 | 1.536E-02 |
| $A_{j,k}^2$ | -6.169 | -1.880E-04 |
| $A_{j,k}^3$ | 18.589 | -1.861E-03 |

maxima have been proposed to be caused by short-range ordering^[32,54] of the liquid around points A and B. Based on the calculated viscosity, the velocity of a TiC_p particle with a diameter of $2.2 \mu\text{m}$ in an Al-Ni binary melt was calculated (Figure 4(d)).

In this study, the temperature at the solidification front was assumed to be the temperature at the liquidus boundary. Thus, the viscosity along the liquidus boundary in Figure 4(a) can be extrapolated as η_{bulk} (Eq. [8]) at the solidification front. The corresponding maximum velocity (V_{cr}) of the TiC_p particle was calculated along the liquidus boundary for various addition of Ni and are shown in Figure 4(d). It should be noted that small additions of Ni in the pure Al melt can significantly retard the movement of a particle during solidification. For example, an addition of 1 wt pct Ni is predicted to increase the viscosity at the liquidus boundary from about 1.1 to 1.6 mPa s (a 45 pct increase) and decrease the maximum velocity (V_{cr}) of the particle from 61.279 to 42.130 $\mu\text{m/s}$ (a 31 pct reduction).

B. Experimental Validation

In this section, the influence of cooling rate and microalloying with 1 wt pct Ni has been experimentally examined for three Al composites, based on the above model. Figure 5(a) shows the size distribution of the TiC_p particles in the pure Al sample. The average particle size was about $1.2 \mu\text{m}$. Figures 5(b) through (d) show the cooling curves at the center and edge position of each die. The corresponding first derivative curves (solidification rate) for these three Al composite samples were calculated. In this study, samples from the center of the die were selected for microstructural observation, because the center of the die has the lowest cooling rate and solidifies last. The average solidification properties [including cooling rate, temperature gradient, and solidification rate (Eq. [20])] at the center of the die were

derived from the liquid–solid region, as shown in Figures 5(b) through (d) and Table IV. The results showed that the average solidification rate of the Al+ TiC_p composite was higher in the 1-cm-diameter die than the 3-cm-diameter die.

The SEM microstructural analysis of the three cast MMC samples is shown in Figure 6. Figure 6(a) shows the microstructure of the first Al + TiC_p sample that was cast into the 3-cm-diameter die, which had a cooling rate of $0.055 \text{ }^\circ\text{C/s}$. A large amount of the TiC_p particles was segregated along the Al grain boundaries. Figures 6(b) and (c) show the microstructure of the second and third Al + TiC_p samples with and without 1 wt pct Ni addition that were cast into the 1-cm-diameter die, which had cooling rates of 0.19 and $0.82 \text{ }^\circ\text{C/s}$, respectively. The serious segregation of particles seen in

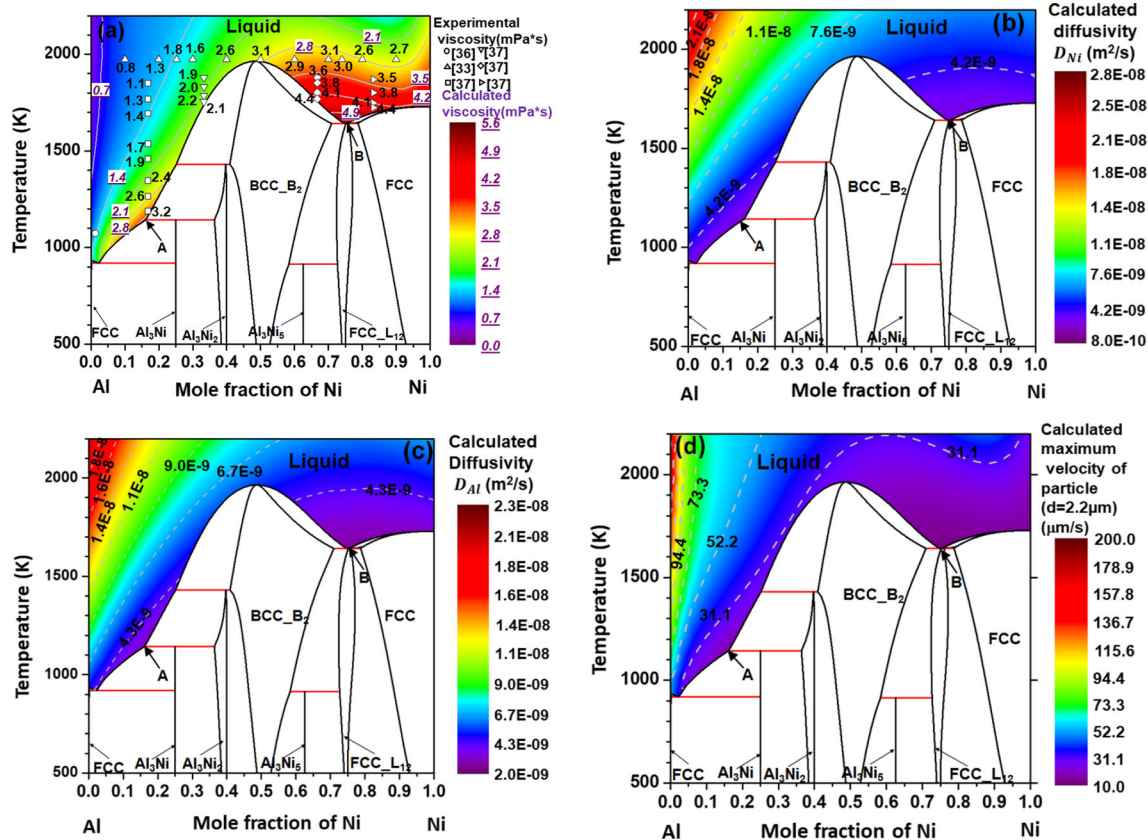


Fig. 4—(a) Calculated viscosity of the Al-Ni binary system above the liquidus boundary superimposed with experimental viscosity data.^[33,36,37] (b, c) Calculated diffusivity of the solute Ni and Al, respectively, in the Al-Ni binary liquid using atomic database.^[53] (d) Calculated corresponding maximum velocity of the ceramic particle (TiC_p) by coupling the capture model and viscosity model. (For interpretation of the references to color in this Figure, the reader is referred to the web version of this article).

Table IV. Solidification Properties of Three Al+ TiC_p Composites With/Without Ni at the Center of Die

| Sample (No.) | MMC System | Average Cooling Rate ($^\circ\text{C/s}$) | Average Temperature Gradient ($^\circ\text{C/cm}$) | Average Solidification Rate ($\mu\text{m/s}$) |
|--------------|--|---|--|---|
| 1st | Al melt—cast in 3-cm-diameter die | 0.055 | 32.10 | 16.98 |
| 2nd | Al melt—cast in 1-cm-diameter die | 0.19 | 51.41 | 36.96 |
| 3rd | Al-1 wt pct Ni—cast in 1-cm-diameter die | 0.82 | 210.02 | 39.05 |

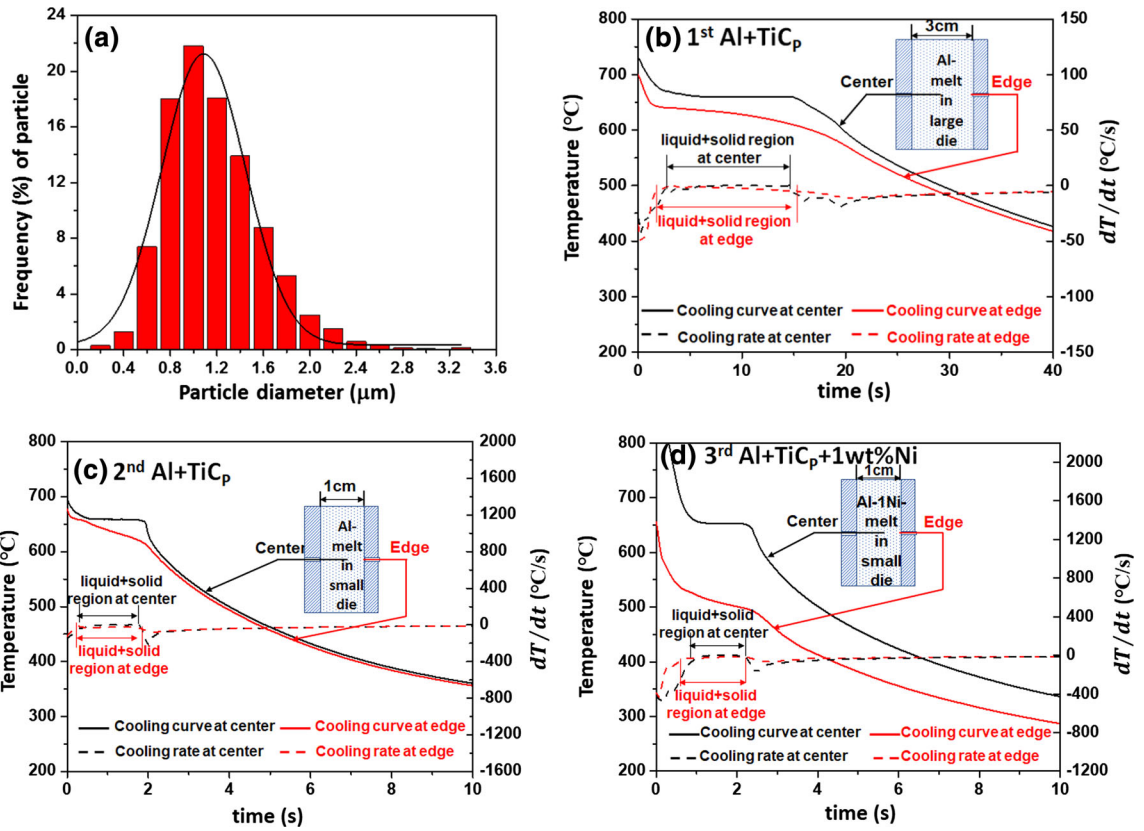


Fig. 5—(a) Size distribution of the ceramic particle (TiC_p) in the pure Al sample used in this work. (b) through (d) Cooling curves and the first derivative curves of first Al + TiC_p composite cast into the 3-cm-diameter die and second Al + TiC_p and third composite Al + TiC_p + 1 wt pct Ni composite cast into the 1-cm-diameter die.

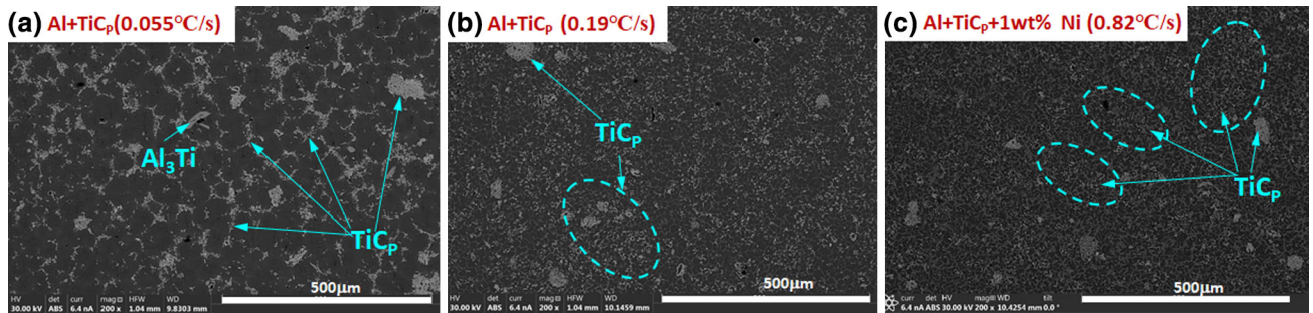


Fig. 6—Microstructure of (a) first Al + TiC_p composite cast into the large die with diameter 3 cm, (b) second Al + TiC_p , and (c) third Al + TiC_p + 1 wt pct Ni composite cast into the small die with diameter 1 cm. Note that all scale bars are 500 μm at 30 kV and 6.4 nA.

Figure 6(a) has been significantly reduced and TiC_p particles have been globally dispersed into the aluminum matrix.

In order to show the local dispersion behavior of TiC_p in the Al matrix, the microstructures of the three samples at higher magnifications are shown in Figures 7(a) through (c). The corresponding experimental solidification rates (V_{SL}) and the calculated maximum particle velocities (V_p) as function of particle size are also shown in Figure 7(d). Figure 7(a) shows that the first sample without Ni additions cast into the

3-cm-diameter die showed a large number of particles segregated along the grain boundaries of the coarse Al grains. The reason could be that the particle size was 400 nm to 3 μm and the corresponding calculated maximum velocity (V_{cr}) of the particles during solidification was 330 $\mu\text{m/s}$ to 60 $\mu\text{m/s}$ (Figure 7(d)). The resulting V_{cr} was higher than the experimental solidification rate ($V_{SL} = 16.98 \mu\text{m/s}$), thus the kinetic criterion for capture was not satisfied and the particles were pushed by the solidification front to the grain boundaries. Figure 7(b) shows a similar phenomenon. TiC_p

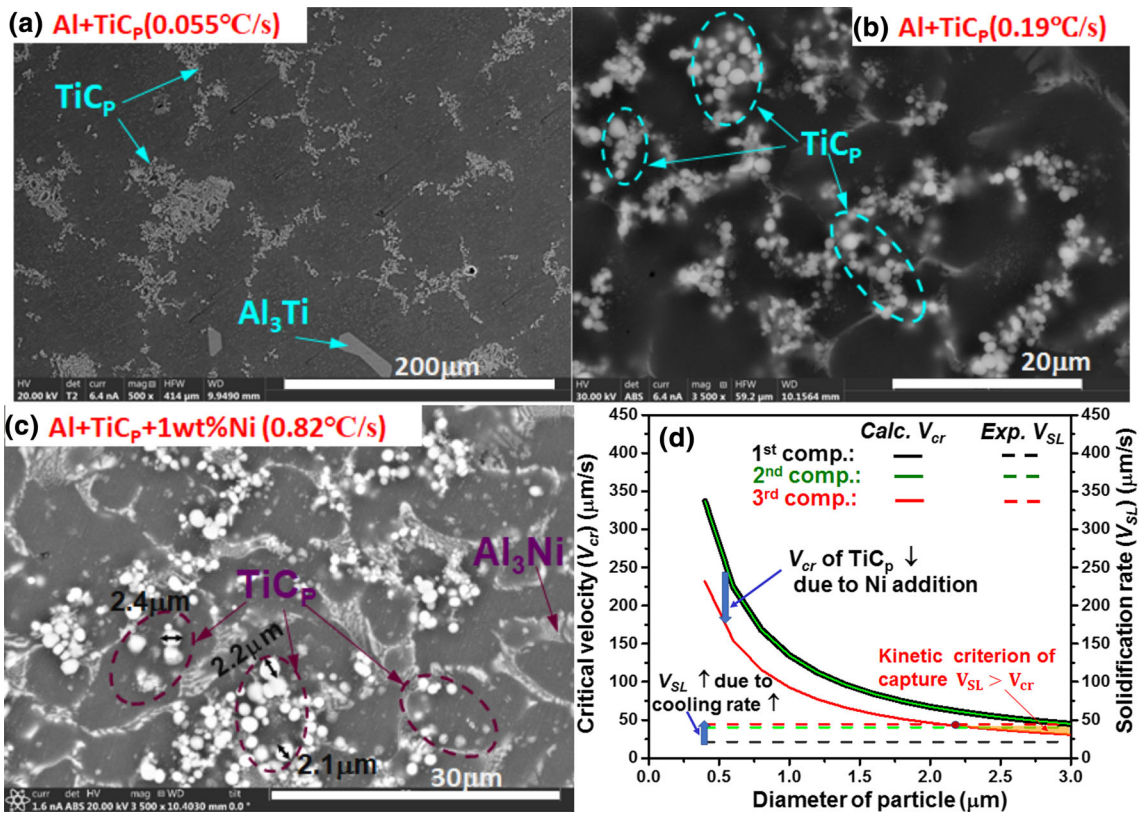


Fig. 7—(a) Local microstructure of the first Al + TiC_p composite cast into the 3-cm-diameter die at 20 kV and 6.4 nA, (b) local microstructure of second Al + TiC_p, at 30 kV and 6.4 nA, and (c) third Al + TiC_p + 1 wt pct Ni composite cast into the 1-cm-diameter die at 20 kV and 1.6 nA, and (d) the calculated velocity (V_{cr}) of TiC_p and experimental solidification rates (V_{SL}) of these three composites during solidification. Note that the (V_{cr}) is the same in 1st and 2nd composites showing overlap lines in (d) because both are pure Al matrix.

particles with a size of 400 nm to 3 μm in pure Al cast in the 1-cm-diameter die were still segregated along the refined grain boundaries. This can be explained by the fact that the experimental solidification rate (V_{SL}) in the 1-cm-diameter die was increased to 36.96 μm/s (Figure 7(d)). However, it was still lower than the maximum velocity (V_{cr}) of particles (330 to 60 μm/s). Thus, the particles should be pushed by the solidification front and trapped along the grain boundaries. It should be noted that the macro-segregation of particles along grain boundaries can be reduced by the refinement of grain size.

Figure 7(c) shows the microstructure of the Al + TiC_p sample with 1 wt pct Ni addition cast into the 1-cm-diameter die. It can be seen that particles > ~ 2 μm in size have been engulfed into the Al grains, while smaller particles (< ~ 2 μm) were still segregated along the grain boundaries. Figure 7(d) shows that the

calculated maximum velocities (V_{cr}) of the particles (400 nm to 3 μm) in the alloy with 1 wt pct Ni were decreased from 230 to 30 μm/s due to the increased viscosity. As a result, the experimental solidification rate (V_{SL} = 39.05 μm/s) was larger than the calculated maximum velocity (V_{cr} = 38.619 μm/s) of the particles > ~ 2 μm in size. The particles > ~ 2 μm in size satisfy the kinetic criterion and should be engulfed into the Al grains. Smaller particles (< ~ 2 μm) were predicted to be pushed to the grain boundaries. Thus, the calculated results in Figure 7(d) from the present particle-capture model were consistent with the experimental observations in (Figures 7(c) and 8(a)). Also, energy-dispersive X-ray spectroscopy (EDS) was performed in Figure 8(b) to characterize the TiC_p particles and grain boundaries with a eutectic intermetallic Al₃Ni phase shown in Figures 8(c) through (f).

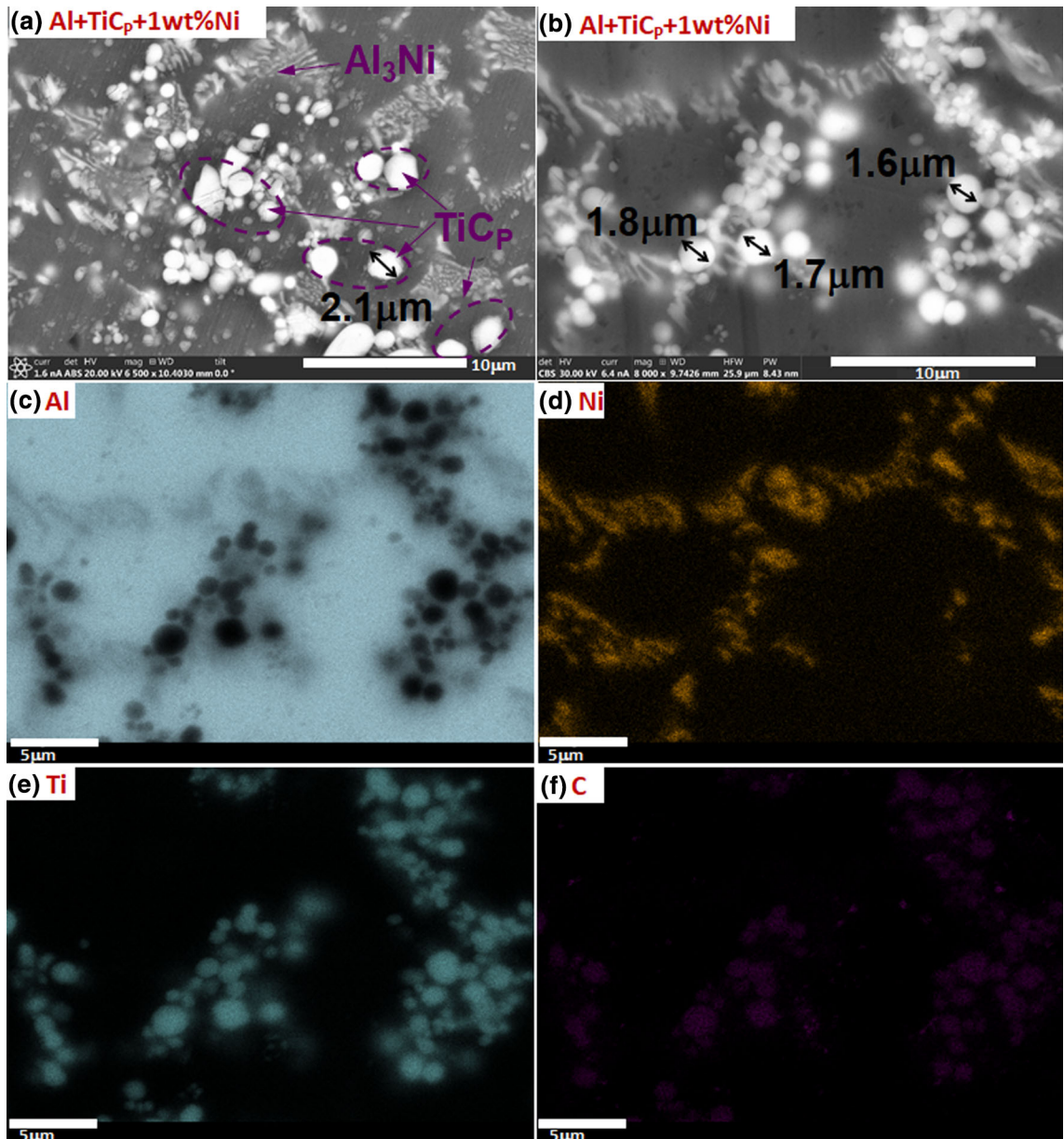


Fig. 8—Local microstructure of Al+TiC_p+1 wt pct Ni composites cast into 1-cm-diameter die with higher magnification: (a) at 20 kV and 1.6 nA; (b) at 30 kV and 6.4 nA. Energy-dispersive X-ray spectroscopy (EDS) of solute (c) Al, (d) Ni, (e) Ti, and (f) C from (b).

IV. CONCLUSIONS

A CALPHAD-based viscosity model has been developed for the binary Al-Ni liquid system using the PARROT module of the Thermo-Calc software. The calculated temperature-dependent viscosities of the unary Ni liquid and the Al-Ni binary alloy system in this study were consistent with available experimental data. A particle-capture model coupled with this viscosity model was developed to study the influence of melt viscosity *via* microalloying of Ni on particle/metal interactions. Finally, the effects of increasing the melt viscosity *via* microalloying with Ni (1 wt pct) and increasing the cooling rate on the maximum particle

velocity during solidification were studied experimentally, with the following conclusions.

1. A CALPHAD-based viscosity model that included the influence of short-range ordering of the liquid was developed and validated to accurately calculate the viscosity of Al-Ni binary melts.
2. A theoretical particle-capture model coupled with the CALPHAD-based viscosity model was developed to study the interactions of the TiC_p particles with aluminum melt during solidification.
3. The solidification rate was increased from 16.98 μm/s in the first composite to 36.96 μm/s in the second composite due to the increase in cooling

rate from 0.055 to 0.19 °C/s. This increase in cooling rate resulted in a reduction in grain size that can be clearly seen between the two Al + TiC_p samples without additions of Ni. Also, the refinement of grain size due to the increased cooling rate reduces the macro-segregation of particles along coarse grain boundaries.

4. Microalloying with 1 wt pct Ni was calculated to increase the viscosity of the pure Al melt by 45 pct at the liquidus boundary and to reduce the critical velocity of TiC_p particles by 31 pct.
5. Due to the 1 wt pct Ni addition and the increase of the cooling rate for the third composite, larger particles ($> \sim 2 \mu\text{m}$) in size were observed to be engulfed into the aluminum grains, while smaller particles ($< \sim 2 \mu\text{m}$) were pushed to the grain boundaries. This is due to the solidification rate (V_{SL}) being higher than the maximum velocity (V_{P}) for the larger particles ($> 2 \mu\text{m}$), but lower than the maximum particle velocity (V_{P}) for smaller particles ($< \sim 2 \mu\text{m}$).

The synergetic approach of (1) increasing cooling rate and (2) increasing viscosity *via* microalloying can be used to improve the engulfment and dispersion of ceramic particles in MMC materials.

ACKNOWLEDGMENTS

The authors gratefully acknowledge the financial support from the Melt R2-2 project funded by LIFT (Lightweight Innovations For Tomorrow), a Manufacturing Institute under the contract from the Office of Naval Research. We thank Prof. Brajendra Mishra and his graduate student Jeremy Fedors (Worcester Polytechnic Institute) for providing the pure Al + TiC_p samples. We also thank graduate students Emre Cinkilic, Yan Lu, and Xuejun Huang (The Ohio State University) for their help with discussions and technical contributions.

REFERENCES

1. T.M. Pollock: *Science*, 2010, vol. 328, pp. 986–87.
2. K. Lu: *Science*, 2010, vol. 328, pp. 319–20.
3. A.I. Taub, P.E. Krajewski, A.A. Luo, and J.N. Owens: *JOM*, 2007, vol. 59, pp. 48–57.
4. A.I. Taub and A.A. Luo: *MRS Bulletin*, 2015, vol. 40, pp. 1045–53.
5. Z. Lu and L. Zhang: *Mater. Des.*, 2017, vol. 116, pp. 427–37.
6. X. Liu, Y. Zhang, B. Beausir, F. Liu, C. Esling, F. Yu, X. Zhao, and L. Zuo: *Acta Mater.*, 2015, vol. 97, pp. 338–47.
7. X. Xia, W. Sun, A.A. Luo, and D.S. Stone: *Acta Mater.*, 2016, vol. 111, pp. 335–47.
8. A.A. Luo, R.K. Mishra, and A.K. Sachdev: *Scripta Mater.*, 2011, vol. 64, pp. 410–13.
9. R. Shi and A.A. Luo: *CALPHAD*, 2018, vol. 62, pp. 1–17.
10. X.L. Zhong, W.L.E. Wong, and M. Gupta: *Acta Mater.*, 2007, vol. 55, pp. 6338–44.
11. L. Jiang, H. Yang, J.K. Yee, X. Mo, T. Topping, E.J. Lavernia, and J.M. Schoenung: *Acta Mater.*, 2016, vol. 103, pp. 128–40.

12. R. Daudin, S. Terzi, P. Lhuissier, J. Tamayo, M. Scheel, N. Hari Babu, D.G. Eskin, and L. Salvo: *Acta Mater.*, 2017, vol. 125, pp. 303–10.
13. W. Zhou, T. Yamaguchi, K. Kikuchi, N. Nomura, and A. Kawasaki: *Acta Mater.*, 2017, vol. 125, pp. 369–76.
14. H. Zhang, H. Springer, R. Aparicio-Fernandez, and D. Raabe: *Acta Mater.*, 2016, vol. 118, pp. 187–95.
15. H. Springer, R. Aparicio Fernandez, M.J. Duarte, A. Kostka, and D. Raabe: *Acta Mater.*, 2015, vol. 96, pp. 47–56.
16. X. Zhang, T. Hu, J.F. Rufner, T.B. LaGrange, G.H. Campbell, E.J. Lavernia, J.M. Schoenung, and K. van Benthem: *Acta Mater.*, 2015, vol. 95, pp. 254–63.
17. L.Y. Chen, J.Q. Xu, H. Choi, M. Pozuelo, X. Ma, S. Bhowmick, J.M. Yang, S. Mathaudhu, and X.C. Li: *Nature*, 2015, vol. 528, pp. 539–43.
18. X. Chen, K.E. Gonsalves, G.M. Chow, and T.D. Xiao: *Adv. Mater.*, 1994, vol. 6, pp. 481–84.
19. I. Kaldre, A. Bojarevics, I. Grants, T. Beinerts, M. Kalvans, M. Milgravis, and G. Gerbeth: *Acta Mater.*, 2016, vol. 118, pp. 253–59.
20. D. Shangguan, S. Ahuja, and D.M. Stefanescu: *Metall. Mater. Trans. A*, 1992, vol. 23, pp. 669–80.
21. D.M. Stefanescu, F.R. Juretzko, B.K. Dhindaw, A. Catalina, S. Sen, and P.A. Curreni: *Metall. Mater. Trans. A*, 1998, vol. 29A, pp. 1697–1706.
22. J.Q. Xu, L.Y. Chen, H. Choi, and X.C. Li: *J. Phys. Condens. Matter*, 2012, vol. 24, pp. 255–304.
23. L.Y. Kozlov, L.M. Romanov, and N.N. Petrov: *Izv. Vuzov. Chernaya. Met.*, 1983, vol. 3, p. 7.
24. G. Kaptay, *Proceedings of MicroCAD 2003 Conference*, Section Metallurgy, University of Miskolc, pp. 23–28.
25. M. Hirai: *ISIJ Int.*, 1993, vol. 33, pp. 251–58.
26. F.J. Cherne and P.A. Deymier: *Scr. Mater.*, 1998, vol. 39, pp. 1613–16.
27. T. Ishikawa, P.-F. Paradis, J.T. Okada, and Y. Watanabe: *Meas. Sci. Technol.*, 2012, vol. 23, pp. 1–9.
28. T. Itami: *Condensed matter–liquid transition metals and alloys in Condensed Matter Disordered Solids*, S.K. Srivastava and N.H. March, eds., World Scientific, Singapore, 1995, pp. 123–250.
29. L. Battezzati and A.L. Greer: *Acta Metall.*, 1989, vol. 37, pp. 1791–1802.
30. Y. Sato, K. Sugisawa, D. Aoki, and T. Yamamura: *Meas. Sci. Technol.*, 2005, vol. 16, pp. 363–71.
31. R.E. Rozas, A.D. Demirag, P.G. Toledo, and J. Horbach: *J. Chem. Phys.*, 2016, vol. 145, p. 064515.
32. N. Jakse and A. Pasturel: *Appl. Phys. Lett.*, 2015, vol. 105, p. 13.
33. M. Kehr, M. Schick, W. Hoyer, and I. Egly: *High Temp.*, 2008, vol. 37, pp. 361–69.
34. I. Egly, R. Brooks, D. Holland-Moritz, R. Novakovic, T. Matsushita, Y. Plevachuk, E. Ricci, S. Seetharaman, V. Sklyarchuk, and R. Wunderlich: *High Temp.*, 2008, vol. 38, pp. 343–51.
35. R.K. Wunderlich and H.J. Fecht: *Int. J. Mater. Res.*, 2011, vol. 102, pp. 1164–73.
36. T. Iida and R.I.L. Guthrie: *The Physical Properties of Liquid Metals*, Clarendon Press, Oxford, 1988.
37. Y. Sato: *Jpn. J. Appl. Phys.*, 2011, vol. 50, p. 11RD01.
38. J. Potschke and V. Rogge: *J. Cryst. Growth*, 1989, vol. 94, pp. 726–38.
39. G. Lefever and A. Jolivet, *Proceedings of International Conference on Heat Exchanger Fouling and Cleaning VIII*, Schladming, Austria, 2009, pp. 120–124.
40. R.B. Bird, W.E. Stewart, and E.N. Lightfoot: *Transport Phenomena*, Wiley, New York, 1960.
41. D.Y.C. Chan and R.G. Horn: *J. Chem. Phys.*, 1985, vol. 83, p. 5311.
42. R.J. Hunter: *The Foundations of Colloid Science*, 2nd ed., Oxford University Press Inc, New York, 2001.
43. F. Zhang, Y. Du, S. Liu, and W. Jie: *CALPHAD*, 2015, vol. 49, pp. 79–86.
44. O. Redlich and A.T. Kister: *Ind. Eng. Chem.*, 1948, vol. 40, pp. 345–48.
45. M.C. Flemings: *Solidification Processing*, McGraw-Hill Inc, New York, NY, 1974, p. 148.

46. M.K. Premkumar and M.G. Chu: *Metall. Mater. Trans. A*, 1993, vol. 24A, pp. 2358–62.
47. R.F. Egerton: *Electron Energy-Loss Spectroscopy in the Electron Microscope*, Springer, New York, 2011, pp. 135–52.
48. X.J. Chen, A.C. Levi, and E. Tosatti: *Surf. Sci.*, 1991, vol. 251, pp. 641–44.
49. R.G. Lye and E.M. Logothetis, *Phys. Rev.*, 1966, vol. 147, pp. 622.
50. J.F. Shackelford and W. Alexander: *Materials Science and Engineering Handbook*, 3rd ed., CRC Press, Boca Raton, 2001, p. 430.
51. D.M. Stefanescu, B.K. Dhindaw, S.A. Kacar, and A. Moitra, *Metall. Mater. Trans. A*, vol. 19A, pp. 2847–55.
52. TCS Aluminium-Based Alloy Thermodynamic Databases TCAL, Version 5, S. Thermo-Calc Software, AB, Sweden (2015).
53. L. Zhang, Y. Du, I. Steinbach, Q. Chen, and B. Huang: *Acta Mater.*, 2010, vol. 58, pp. 3664–75.
54. A. Pasturel, N. Jakse, and J. Non-Cryst: *Solids*, 2015, vol. 425, pp. 176–82.

Publisher's Note Springer Nature remains neutral with regard to jurisdictional claims in published maps and institutional affiliations.